DOI: 10.1002/((please add manuscript number))
Article type: Communication

Giant Rashba Splitting in $Pb_{1-x}Sn_xTe$ (111) Topological Crystalline Insulator Films Controlled by Bi-Doping in the Bulk

V. V. Volobuev[1,2]*, P.S. Mandal[3], M. Galicka[5], O. Caha[4], J. Sanchez-Barriga[3], D. Di Sante[6,7], A. Varykhalov[3], A. Khiar[1], S. Picozzi[6], G. Bauer[1], P. Kacman[5], R. Buczko[5], O. Rader[3], and G. Springholz[1]*

[1] Dr. V. V. Volobuev, Dr. A. Khiar, Prof. G. Bauer, Prof. G. Springholz, Institute for Semiconductor Physics, Johannes Kepler University, Altenberger Str. 69, 4040 Linz, Austria

[2] Dr. V. V. Volobuev, National Technical University "Kharkiv Polytechnic Institute", Frunze Str. 21, 61002 Kharkiv, Ukraine

[3] P.S. Mandal, Dr. J. Sanchez-Barriga, Dr. A. Varykhalov, Prof. O. Rader, Helmholtz-Zentrum Berlin, Elektronenspeichering BESSY II, Albert-Einstein Str. 15, 12489 Berlin, Germany

[4] Dr. O. Caha, Masaryk University, Kotlářská 2, 61137 Brno, Czech Republic

[5] Dr. M. Galicka, Prof. P. Kacman, Prof. R. Buczko, Institute of Physics, Polish Academy of Sciences, Aleja Lotników 32/46, PL-02-668 Warszawa, Poland

[6] Dr. D. Di Sante, Dr. S. Picozzi, Consiglio Nazionale delle Ricerche CNR-SPIN, Via dei Vestini 31, 66100 Chieti, Italy

[7] Dr. D. Di Sante, Institut für Physik und Astrophysik, Universität Würzburg, Am Hubland Campus Süd, Würzburg 97074, Germany

*) e-mail: valentyn.volobuiev@jku.at, gunther.springholz@jku.at

Keywords: Topological crystalline insulators, IV-VI semiconductors, angle resolved photoemission spectroscopy, molecular beam epitaxy, Rashba effect

TOC Abstract: Topological crystalline insulators such as $Pb_{1-x}Sn_xTe$ have attracted great interest due to the wide tunability of the topological properties through temperature and composition. Here we show that bulk Bi-doping of epitaxial $Pb_{1-x}Sn_xTe$ (111) films induces a giant Rashba splitting of the surface state that can be tuned by the doping level. Tight binding calculations identify its origin as Fermi level pinning by trap states at the surface.

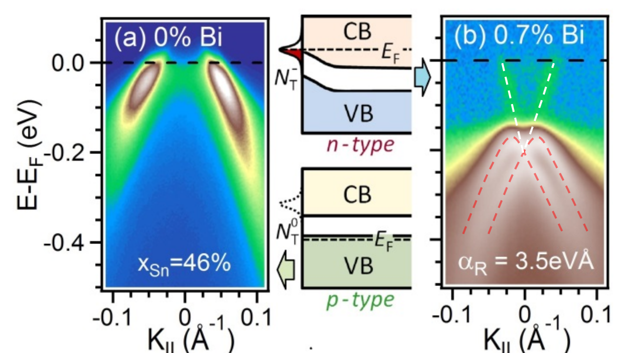

Introduction

A novel class of topological insulators (TI), called topological crystalline insulators (TCI), has been recently predicted[1,2] and experimentally demonstrated for SnTe[2,3], $Pb_{1-x}Sn_xTe$[4,5] and $Pb_{1-x}Sn_xSe$[6]. In these IV-VI materials, an inversion of the L_{6+} and L_{6-} valence and conduction bands occurs above a certain critical Sn content (see Figure 1a)[7–9]. This induces a trivial to non-trivial topological phase transition which, due to the bulk-surface connectivity, gives rise to the formation of a two-dimensional (2D) topological surface state (TSS) with linear dispersion of a Dirac cone and helical spin texture due to spin-momentum locking[1,2,6],[10–12]. In TCIs these topological surface states are protected by crystal mirror symmetries[1,2] rather than by time reversal symmetry as in conventional Z_2 topological insulators[13,14]. Thus, these surface states are formed on particular surfaces such as (001), (111) and (110) where the crystalline mirror symmetries are preserved[1,2],[12]. Moreover, the band inversion is highly sensitive to external perturbations[10],[15],[16]. Therefore, the topological trivial to non-trivial transition of TCIs can be controlled by many different means, such as by varying temperature[1,6], pressure[2], hybridization in ultrathin film geometries[17–19], magnetic interactions[20] or by breaking of mirror symmetries by strain[16,21–23], electrostatic fields[18] or ferroelectric lattice distortions[24,25]. This provides ample degrees of freedom for topology control not available in conventional Z_2 TIs. For this reason, TCIs offer an ideal template for observation of exotic phenomena such as partially flat band helical snake states and interfacial superconductivity,[16] large-Chern-number quantum anomalous Hall effect[26], as well as for realization of novel topology-based devices such as topological photodetectors[23], spin transistors[18] and spin torque devices[27].

For most of such applications, thin film structures with precisely controlled composition and Fermi level are required. Up to now, most work has been performed on highly *p*-type bulk crystals exploiting the natural (001) cleavage plane of the IV-VI compounds[3,4,6], whereas for other surface orientations and actual devices epitaxial TCI film structures are required[18,28–32]. The (111) orientation is particularly interesting due to the polar nature of its surface[12] as well as the ease of lifting the four-fold valley degeneracy at the *L*-points of the Brillouin zone (BZ) [33] by opening a gap at particular Dirac points by strain[16] and quantum confinement[17–19] to induce a transition from a TCI to a normal Z_2-TI material[25]. Epitaxial growth strongly relies on lattice- and thermal expansion matching between films and substrate material. Good results have been obtained, e.g., for PbSnTe on Bi_2Te_3 buffer layers,[31,34] but corresponding transport and angle resolved photoemission (ARPES) investigations are offset by the intrinsic topological character of Bi_2Te_3[31,35] as well as by PbSnTe/Bi_2Te_3 interdiffusion

and intermixing. Most challenging, however, is the intrinsic *p*-type character of PbSnTe caused by the natural tendency of cation vacancy formation, creating resonant acceptor levels in the valence band[9]. This tendency strongly increases with increasing Sn content and thus, SnTe always exhibits very high bulk hole concentrations above 10^{20} cm^{-3}. This not only masks the topological surface state in transport and optical investigations but also impedes observing the Dirac point by ARPES.

In the present work, we employ molecular beam epitaxy to grow high quality $Pb_{1-x}Sn_xTe$ films in which *extrinsic n*-type doping is employed for compensation and control of carrier concentration. We show that Bi doping allows to tune the Fermi level over a wide range from the valence to the conduction band and thus to observe the trivial to nontrivial topological transition under temperature and composition variation. By careful tuning of the doping level and growth conditions, low free carrier concentrations of 10^{18} cm^{-3} and carrier mobilities as high as 10^4 cm^2/Vs are achieved, providing excellent conditions for quantum transport and optical studies of non-trivial topology effects[32]. *Most strikingly, we find that Bi-doping induces a very large Rashba splitting of the valence band* that is absent for undoped material and reaches values as high as 0.022 $Å^{-1}$. This yields a giant Rashba coupling constant of 3.8 eVÅ that is comparable to the record values recently reported for the BiTe-halide compounds[36],[37],[38]. Our tight binding calculations reveal that this Rashba splitting is caused by pinning of the Fermi level due to acceptor like surface states. The important outcome is that the Rasbha effect can be tailored and tuned by bulk Bi-doping. The coexistence and hybridization of TSS and Rashba-split surface states is unexpected due to the inversion symmetry of the rock salt structure and paves the way for novel topological spin-orbitronic devices[39].

Results

Epitaxial growth of $Pb_{1-x}Sn_xTe$ was performed by molecular beam epitaxy on BaF_2 (111) substrates using stoichiometric PbTe and SnTe beam flux sources[40],[41]. The chemical composition of the layers was varied over a wide range from x_{Sn} = 0 to 1 by control of the SnTe/PbTe beam flux ratio, which was measured precisely using the quartz crystal microbalance method[40]. *N*-type doping was realized using a Bi_2Te_3 compound source to promote substitutional incorporation of bismuth into cation lattice sites[42] where Bi acts as donor because of its additional valence electron compared to Pb or Sn[42,43]. The solubility of Bi_2Te_3 in SnTe and PbTe amounts to several percent according to the quasi binary phase diagrams[44]. For compensation of the native *p*-type carrier concentration, however,

only small Bi concentrations and Bi flux rates in the 10^{-4} – 10^{-3} monolayer (ML)/s range are required, compared to overall film growth rates of 1 ML/s (=3.7Å/s) used in our case.

2D growth of $Pb_{1-x}Sn_xTe$ (111) films is observed for all compositions beyond a thickness of 100 nm as demonstrated by the reflection high-energy electron diffraction (RHEED) patterns and atomic force microscopy (AFM) image depicted in Figures 1b,c for x_{Sn} = 0.4. The high film quality is evidenced by sharp diffraction spots arranged on the Laue circle and the intense Kikuchi lines arising from scattering at subsurface lattice planes. No surface reconstruction is observed. The surface is atomically flat exhibiting about 200 nm wide terraces separated by single monolayer steps of 3.7Å height (*cf*. Figure 1d). At the given substrate temperature of 350°C, growth proceeds in a step-flow mode with the surface steps pinned by threading dislocations as described in detail in Refs. [45],[46]. Structural characterization by high resolution x-ray reciprocal space mapping (see Figures 1e-g) demonstrates that the layers with 1 – 2 µm thickness are fully relaxed. Accordingly, their Bragg peaks lie exactly along the line connecting the bulk PbTe (a_{PbTe}=6.462Å) and SnTe (a_{SnTe}=6.323Å) reciprocal lattice points, as indicated by the dashed and solid lines, respectively. Thus, the epilayers are undistorted with equal in- and out-of-plane lattice constants. Systematic evaluation of the lattice parameters as a function of composition shows that it precisely follows Vegard's law[47]. In particular, for all samples the Sn content derived by x-ray diffraction perfectly agrees with the nominal growth values. Moreover, no traces of any secondary phases were detected.

The Bi doping action and transport properties were evaluated by Hall effect measurements as summarized in Figure 2. Undoped PbTe layers are *n*-type in the low 10^{17} cm^{-3} range under stoichiometric MBE growth conditions[40,42]. On the contrary, the carrier type of $Pb_{1-x}Sn_xTe$ switches from *n* to *p*-type at x_{sn} > 15% and thereafter the hole concentration rises exponentially with increasing Sn content, reaching hole densities as high as 2×10^{20} cm^{-3} for pure SnTe (see Figure 2a). This demonstrates an exceedingly low cation vacancy formation energy E_V of SnTe compared to PbTe.[48] For undoped $Pb_{1-x}Sn_xTe$ TCI films requiring x_{Sn} larger than 40%, the Fermi level is therefore always deep in the valence band[3–5], [33]. We model the dependence of the cation vacancy formation energy on composition using $E_V(x_{Sn}) = E_{V,SnTe} + \Delta E_V(1 - x_{Sn})$, where ΔE_V is the vacancy energy difference between PbTe and SnTe. Assuming an Arrhenius-like behavior for the equilibrium vacancy concentration, the native free carrier concentration in $Pb_{1-x}Sn_xTe$ is predicted as:

$$n_{n,p}(x_{Sn}) = -n_{n,PbTe} + n_{p,SnTe}e^{-\Delta E_V(1-x_{Sn})/kT} \quad (1)$$

where $n_{n,PbTe}$ and $n_{p,SnTe}$ are the intrinsic carrier concentrations of the parent binary materials for the given growth conditions. As demonstrated by the solid line in Figure 2(a), this model perfectly describes our experimental findings and from the fit of our data, a difference in the cation vacancy formation energy between PbTe and SnTe of ΔE_v = 360 meV is derived.

Effective control of the carrier type and tuning of the carrier concentration by Bi doping is demonstrated by Figure 2b, where the Hall concentrations of Bi-doped PbTe (◆) and $Pb_{0.54}Sn_{0.46}Te$ (■,●) epilayers are plotted versus Bi concentration. For PbTe, the electron concentration rises perfectly linearly with Bi dopant concentration (solid line), evidencing a single ionized donor state and a unity doping efficiency $\gamma = (n - n_0) / n_{Bi}$ for Bi concentrations as high as 10^{20} cm^{-3}. This provides a precise calibration of the Bi flux for growth. For $Pb_{0.54}Sn_{0.46}Te$, Bi doping partially compensates the native hole concentration until for $n_{Bi} > 2\times10^{19}$ cm^{-3} the material switches from *p* to *n*-type with electron concentrations up to the mid-10^{19} cm^{-3} range (*cf*. Fig. 2b). Thus, the carrier density can be tuned over a wide range. By precise control of the Bi flux, low carrier densities within the 10^{17} cm^{-3} range can be obtained, resulting in Hall mobilities as high as μ_H = 13000 cm^2/Vs at 77 K, comparable or even exceeding the highest values reported for long term annealed bulk single crystals[49]. Inspection of Figure 2b reveals, however, that for high-doped $Pb_{0.54}Sn_{0.46}Te$ films the actual electron concentration is significantly below the expected values for γ = 1 (dashed line) and that the maximum electron concentration saturates in the mid 10^{19} cm^{-3} range even at high Bi concentrations. This means that the doping efficiency decreases with increasing Sn content to $\gamma < 0.4$ for x_{Sn} = 46% (Figure 2c), whereas for pure PbTe it is unity for all investigated Bi concentrations. This suggests that Bi develops an amphoteric character in the ternary materials and starts to occupy Te lattice sites as well, on which it acts like an acceptor. Thus, compensation of the native hole concentration becomes increasingly difficult at higher Sn contents.

The effect of Bi-doping on the topological surface state and population of the electronic bands is studied in detail by angle resolved photoemission spectroscopy as a function of temperature and composition in the 17 – 90 eV photon energy range. As shown by Figure 3, for *n*-doped $Pb_{0.54}Sn_{0.46}Te$:Bi films both conduction and valence bands are clearly visible in ARPES, whereas for undoped films only the lower branch of the valence band is seen because the Fermi level is well below the valence band (VB) edge (see Figure 4a). For a Bi doping of n_{Bi} = 4 x 10^{19} cm^{-3} (=0.3% Bi), the Fermi level E_F at room temperature is already by +100 meV above the conduction band (CB) edge and

lowering the temperature induces a further upward shift to +160 meV at 110 K (*cf*. Fig. 3a-c). At this temperature a pronounced 2D topological surface state with linear dispersion appears, indicating the transition from the trivial to the non-trivial TCI state. Also, an increase in the Fermi velocity, i.e., slope of the $E(k)$ dispersion occurs due to the decrease of the effective masses accompanying the closing of the gap[8,9]. This in turn leads to a decrease in the electronic density of states, which means that the Fermi energy must shift upwards at lower temperatures to accommodate the temperature independent, i.e., constant carrier concentration as observed by the Hall effect measurements.

The 2D nature of the observed surface state was verified by photon energy dependent ARPES investigations shown in Figure 3e-h. In spite of different admixtures of dispersive bulk and non-dispersive surface signals at different photon energies, the absence of any photon energy dispersion corroborates that the observed bands are indeed surface states with 2D character. For the *n*-doped $Pb_{0.54}Sn_{0.46}Te$ films, linear extrapolation of the TSS from the conduction band yields a Dirac point position at 10 - 20 meV below the VB maximum at 110K. This is revealed clearly by Figure 3j,k where the ARPES intensity is depicted on a logarithmic scale. Also shown for comparison is the ARPES data of a film with x_{Sn} = 26%, in which the gap remains fully open with E_g ~120 meV even at low temperatures, i.e., for low Sn contents $Pb_{1-x}Sn_xTe$ remains topologically trivial. Thus, the trivial to non-trivial topological phase transition is demonstrated for (111) epitaxial films both as a function of temperature and Sn content. It is noted that the topological phase transition was previously suggested to occur already at $x_{sn} \approx 0.25$ for cleaved (001) bulk $Pb_{1-x}Sn_xTe$ crystals.[5] However, this conclusion was based only on extrapolation of the dispersion of the valence band of highly *p*-type material without directly observing the Dirac point and conduction band.

Remarkably, all *n*-doped films show a very large Rashba splitting of the valence band in the k_{II} direction. To map out the correlation with the doping level, ARPES was performed for a series of $Pb_{0.54}Sn_{0.46}Te$ layers with systematically increasing doping level. The results are presented in Figure 4 for Bi concentrations varying from 0 to 1%. Whereas for the undoped film the Fermi level is deep inside the VB it strongly moves upward with increasing Bi content such that for $n_{Bi} > 0.2\%$, the full VB dispersion and CB appears. In fact, a total shift of E_F by as much +280 meV is achieved by 1% Bi doping, evidencing the effective control of the Fermi level. Most importantly, we find that the Rashba splitting systematically increases with the Bi concentration. Thus, the Rashba effect is induced by the *bulk doping* of the material, which is in complete contrast to the Rashba effect in Z_2-topological insu-

lators such as Bi_2Se_3, which is usually induced by alkaline[50],[51] or transition metal deposition [52] or adsorption of water on the surface[53],[54], but not upon bulk doping[52],[55],[56],[57],[58],[59]. Moreover, it is to be noted that in these Z_2-TIs the Rashba bands are completely separated in energy from the topological surface state, whereas in our TCI case the Dirac and Kramers point overlap (see Figure 3j). This suggests that a strong a hybridization between the TSS and the Rashba bands may occur.

For quantitative evaluation, the Rashba bands were modeled using the effective mass approximation where the energy-momentum dispersions is given by

$$E(k_{\pm}) = \hbar^2 k^2/2m^* + \alpha_R(\vec{\sigma} \times \hat{k})\hat{z} = \hbar^2 k^2/2m^* \pm \alpha_R k \qquad (2)$$

where m^* is the effective carrier mass in the k_{II} direction, σ the Pauli spin matrix and α_R the Rashba constant due to spin-orbit coupling and structural asymmetry at the surface. The Rashba effect causes the formation of two separate spin polarized bands k_+ and k_- that are splitted by $2\Delta k_R$ in the k_{II} direction, as indicated schematically by the dashed lines in Figure 4d. This leads to a nested band structure with helical spin texture, forming concentric rings in the k_{xy} plane as corroborated by the constant energy ARPES maps depicted in Figure 4e-h. This is a key hallmark of the Rashba effect. From the data, we derive the momentum splitting Δk_R and Rashba energy E_R (= energy difference between the band maxima and the Kramers point) for each sample, which yields the Rashba coupling constant $\alpha_R = 2E_R/\Delta k_R$ as a function of the doping level. The results are summarized in Table 1, demonstrating a clear correlation between the Rashba parameters and Bi concentration. In particular, the Rashba constant assumes exceedingly large values of α_R = 3.8 eVÅ for 1% Bi-doping, which is comparable to the recently reported record values of the giant Rashba systems such as BiTe*X* (*X*=I, Br, and Cl) and α-GeTe where α_R is of the order of 2 – 4 eVÅ [36–38],[60–63].

The giant Rashba splitting is quite unexpected for materials possessing inversion symmetry as applies for the IV-VI compounds with cubic rock salt crystal structure. As recently suggested, ferroelectric (FE) lattice distortions can lead to a giant bulk Rashba splitting[60] in α-GeTe[62,63] and SnTe[25]. In our $Pb_{1-x}Sn_xTe$ films, however, we do not observe such distortions by x-ray diffraction down to 80K, and even pure SnTe becomes ferroelectric only at low temperatures. Moreover, for films we don´t observe any abrupt change of the Rashba effect with temperature (*cf*. Figure 3) as would be expected at such a FE phase transition. Thus, we rule out bulk inversion symmetry breaking and the Dresselhaus mechanism as an origin for our Rashba effect. Instead, we invoke a symmetry breaking at the surface.

In fact, the mere existence of the surface can produce spin polarized surface states, as has been shown in the case of $Pb_{0.73}Sn_{0.27}Se$ in the normal insulator phase[47]. A surface band bending can tune these states to the band gap region, and/or produce new states localized at the surface and enhance the spin splitting. The pertaining Rashba effect will be thus confined to the surface, in agreement with the observed 2D nature of the Rashba bands revealed by the photon energy dependence (Figure 3). We suggest that the surface band bending for PbSnTe (111) is caused by a pinning of the Fermi level by localized trap states at the surface due to dangling bonds. This results in the presence of a fixed surface charge σ_S that induces a depletion layer below the surface. For degenerately doped semiconductors this is described by the Thomas Fermi screening model with a screening potential of

$$V(z) = V_0 \exp(-z/\lambda) \qquad (3)$$

where V_0 is the potential at the surface at z = 0 and $\lambda = \pi^{2/3}\hbar\sqrt{\varepsilon_0\varepsilon_s/e^2m^*(3n)^{1/3}}$ is the Thomas Fermi screening length[64], which is of the order of a few nanometers for highly doped semiconductors. The surface potential V_0 is related to the surface charge by $V_0 = -\sigma_S \lambda/\varepsilon_0\varepsilon_s$ through the Poisson´s equation and the overall charge neutrality condition. For acceptor-like trap states, the trapped surface charge σ_S is negative so that the bands bend upwards at the surface and V_0 assumes a positive value. Likewise, for donor-like surface states σ_S is positive, inducing a downward band bending corresponding to negative V_0 values.

The effect on the surface spectral density of states was evaluated by tight binding calculations in which on the atomic potentials of $Pb_{0.54}Sn_{0.46}Te$ obtained in Refs. [6] and [12] different surface band bending potentials according to Eq. 3 were superimposed. We assume an anion (Te) termination of the (111) surface as DFT calculations[48] suggest that this surface exhibits a lower surface energy than the cation termination. The results are presented in Figure 4 for λ = 2.5 and V_0 varying from -0.5, +0.3 and +0.1 eV from (j) to (l), respectively, where the solid lines correspond to the 2D surface states and the shaded regions to the bulk bands. Evidently, surface band bending induces a strong Rashba splitting in either the CB or VB depending on the *sign* of V_0. Positive V_0 (i.e., upward band bending) leads to a Rashba splitting in the VB due to the confinement of the hole wave functions near the surface. Conversely, for negative V_0 the Rashba splitted states appear in the CB. Comparison with our experiments reveals that only the upward band bending, i.e., $V_0 > 0$ is consistent with the ARPES data, which demonstrates the presence of a negative surface charge σ_S on the anion terminated surface.

From our TB calculations, we derive the dependence of Rashba parameters as a function of surface potential as presented in Figure 4m. Evidently, the momentum splitting Δk_R and Rashba constant scale linearly, and E_R quadratically with the surface potential V_0, i.e., with increasing electric field strength $\mathcal{E} \sim dV/dz$ at the surface. Comparison with the experimentally values indicates a surface potential V_0 of around +0.1 to +0.3 eV for our samples, which for the given screening length and dielectric constant yields a surface charge of the order of 1/10 electron per surface atom. However, the observed increase of the Rashba splitting with increasing Bi-doping dictates that this surface charge is *not constant* but varies with the bulk Fermi level. Thus, it cannot be simply due to the polar nature of the (111) surface as previously suggested[65], but rather by localized surface trap states that are successively filled by electrons as the bulk Fermi level increases. For *p*-doped samples these trap states are unoccupied, corresponding to a flat band condition (cf. insert of Fig. 4i) without a Rashba effect - as seen in our experiments. Comparing calculated and measured Rashba parameters, we find a good agreement for $V_0 = +0.2$ eV where α_R is of the order of 3 eVÅ in both theory and experiment. The upward surface band bending also nicely explains the weak intensity of the CB band states in the ARPES measurements because accordingly the CV wave functions are pushed into the bulk away from the surface and thus, their spectral weight at the surface is strongly reduced. Also note that for a given α_R value, Δk_R and E_R of the TB calculations are somewhat smaller than the experimental values. Since both are proportional to the in-plane effective mass m^*, this is attributed to fact that m^* is underestimated by a factor of 1.8 in the TB binding calculations as compared to the experiments. The effect of temperature and screening length variation is discussed in the supplemental information.

It is well known that Bi on metal surfaces can induce a large Rashba splitting due to its large spin-orbit coupling, as e.g., for Bi/Ag(111) surface alloys.[66,67]To rule out such an effect, we have deposited 0.5 - 1 monolayer of Bi on top of undoped $Pb_{0.54}Sn_{0.46}Te$ (111) at a temperature of 200K. The resulting ARPES data, shown in supplemental Figure S1[68] reveals that this does not cause *any* Rashba splitting of the PbSnTe bands. This corroborates that simple Bi accumulation on the PbSnTe surface, e.g. by surface segregation would not explain our Rashba effect. This is further underlined by the core level spectra of our bulk-doped films in Figure 4i, which show that the surface concentration of Bi remains very small in all samples and that no notable Bi accumulation occurs. To further demonstrate that the Rashba effect also does not rely on any specific property of the Bi dopant, we have prepared $Pb_{0.54}Sn_{0.46}Te$ films where Bi was replaced by Sb as group V *n*-type dopant. As shown by the supplemental Figure S1 [68], for such films a similar giant Rashba effect is observed. In fact, for a nom-

inal Sb concentration of 3% we obtain an even larger Rashba splitting of Δk_R = 0.036 $Å^{-1}$ and E_R = 56 meV as compared to the 1% Bi doped sample. This clearly corroborates that the Rashba effect is solely controlled by the bulk Fermi level and thus will occur for any other *n*-type dopant of the system.

Summary

In summary, we have shown that Bi- and Sb-doped topological crystalline insulator $Pb_{1-x}Sn_xTe$ (111) films represent a giant Rashba system that features Rashba coupling constant as high as the record values reported in literature. Contrary to most other systems, the strength of the Rashba effect is effectively controlled by the bulk doping. Our detailed analysis using tight binding calculations reveals that it originates from a large upward band bending at the surface due to electron surface traps, whose occupancy is controlled by the bulk Fermi level. Since the Fermi level can be also tuned by electrostatic gates, this opens up a pathway for spintronic field effect device applications. Doping also allows compensating the intrinsic *p*-type character of TCI materials, resulting in high carrier mobilities that enables optical and topological quantum transport investigations otherwise screened by the bulk contribution. The magnitude of spin-splitting seems certainly sufficient for room temperature operation of spintronic devices based on spin-galvanic effects [39,69–71], but beyond that our observed trends imply that the spin-splitting can be even further enhanced by increased Bi or Sb doping levels. Thus, our findings open up new avenues for exploring exotic electrical and optical phenomena in topological systems as well as novel spintronic devices driven by the Rashba effect.

Method Section

Sample Preparation: Bi-doped $Pb_{1-x}Sn_xTe$ thin films were grown in a Varian Gen II MBE system on cleaved (111) BaF_2 substrates at 350 ºC at a pressure below 10^{-9} mbar. The film growth was in-situ monitored by RHEED. PbTe, SnTe and Bi_2Te_3 were evaporated from compound effusion cells. In some cases, a $Pb_{0.44}Sn_{0.56}Te$ stoichiometric source was used. The PbTe/SnTe/Bi ratio was controlled and calibrated by a quartz crystal microbalance moved into the substrate position. The thickness of the films was in the range of 1 – 2 µm.

Sample Characterization: The surface of grown films was examined by AFM in contact mode. X-ray diffraction measurements and reciprocal space maps were performed using a double crystal Seifert 3003 diffractometer equipped with a channel cut Ge (200) monochromator. The composition was determined using the Vegards law as well as energy dispersive x-ray microanalysis and photoelectron spectroscopy.

Transport Characterization: Hall measurements were carried out in Van der Pauw geometry with external magnetic fields up to 0.9 Tesla. Measurements were performed and room temperature and liquid nitrogen. Selected samples were also measured in high magnetic fields up to 7 T at 1.7K. The obtained high field and low field carrier concentrations are consistent with each other within 20%.

ARPES Measurements: Angle-resolved photoemission was measured at UE112_PGM-2a-1^2 beam-line at the Bessy II synchrotron (Berlin, Germany) with photon energies ranging from 15-90 eV and horizontally polarized light using a six-axes automated cryo-manipulator and Scienta R8000 detector with typical energy resolution better than 5 meV. For these investigations, the as grown samples were transferred from the MBE to the synchrotron using a battery operated ion getter pumped UHV suitcase (Ferrovac VSN40S) sustaining a base pressure better than 2×10^{-10} mbar. The ARPES experi-ments were carried out at pressures below 2×10^{-10} mbar.

Theoretical Calculations: The surface spectral density of states in the studied $Pb_{0.54}Sn_{0.46}Te$ films was obtained using the tight-binding approach within the virtual crystal approximation. The parameters for the constituent compounds, PbTe and SnTe were taken from Ref. [72], where they were obtained within a nearest neighbor 18-orbital sp^3d^5 model with spin-orbit interactions included. To obtain a correct dependence of the band gap with temperature we had, however, to find an appropriate scal-ing of the hopping integrals with temperature. The Bi incorporation was simulated by applying a sur-

face potential described by equation (3) within the Thomas Fermi screening model. The surface spectral functions have been calculated using recursive Green's function method described in Ref. [73].

Acknowledgements

We acknowledge the Helmholtz-Zentrum Berlin for provision of synchrotron radiation beamtime at UE112_PGM-2a-1^2 of BESSY II, and thank Prof. E.I. Rogacheva, National Technical University "KhPI" Kharkiv, Ukraine and Dr. A. Szczerbakow, Institute of Physics of the Polish Academy of Sciences in Warszawa for providing the MBE source material. This work was supported by the Austrian Science Funds (grant SFB 025-IRON), the EU CALIPSO (grant number 312284), and the Polish National Science Center (grants No. 2013/11/B/ST3/03934 and 2014/15/B/ST3/03833). Tight binding calculations were partially carried out in the Academic Computer Center in Gdansk.

Received: ((will be filled in by the editorial staff))
Revised: ((will be filled in by the editorial staff))
Published online: ((will be filled in by the editorial staff))

References

[1] L. Fu, *Phys. Rev. Lett.* **2011**, *106*, 106802.

[2] T. H. Hsieh, H. Lin, J. Liu, W. Duan, A. Bansi, L. Fu, *Nat. Commun.* **2012**, *3*, 982.

[3] Y. Tanaka, Z. Ren, T. Sato, K. Nakayama, S. Souma, T. Takahashi, K. Segawa, Y. Ando, *Nat. Phys.* **2012**, *8*, 800.

[4] S.-Y. Xu, C. Liu, N. Alidoust, M. Neupane, D. Qian, I. Belopolski, J. D. D. Denlinger, Y. J. J. Wang, H. Lin, L. A. a. Wray, G. Landolt, B. Slomski, J. H. H. Dil, A. Marcinkova, E. Morosan, Q. Gibson, R. Sankar, F. C. C. Chou, R. J. J. Cava, a. Bansil, M. Z. Z. Hasan, *Nat. Commun.* **2012**, *3*, 1192.

[5] Y. Tanaka, T. Sato, K. Nakayama, S. Souma, T. Takahashi, Z. Ren, M. Novak, K. Segawa, Y. Ando, *Phys. Rev. B - Condens. Matter Mater. Phys.* **2013**, *87*, 155105.

[6] P. Dziawa, B. J. Kowalski, K. Dybko, R. Buczko, A. Szczerbakow, M. Szot, E. Łusakowska, T. Balasubramanian, B. M. Wojek, M. H. Berntsen, O. Tjernberg, T. Story, *Nat. Mater.* **2012**, *11*, 1023.

[7] W. D. Johnston, J. G. King, R. Sci, I. Estermann, O. C. Simpson, O. Stern, H. S. W Massey, C. B. O Mohr, P. Roy, J. O. Dimmock, I. Melngailis, A. J. Strauss, *Phys. Rev. Lett.* **1966**, *16*, 1193.

[8] H. Preier, *Appl. Phys.* **1979**, *20*, 189.

[9] G. Nimtz, B. Schlicht, in *Narrow-Gap Semicond.*, Springer-Verlag, Berlin/Heidelberg, **1983**, pp. 1–117.

[10] Y. Ando, L. Fu, *Annu. Rev. Condens. Matter Phys.* **2015**, *6*, 361.

[11] B. M. Wojek, R. Buczko, S. Safaei, P. Dziawa, B. J. Kowalski, M. H. Berntsen, T. Balasubramanian, M. Leandersson, A. Szczerbakow, P. Kacman, T. Story, O. Tjernberg, *Phys. Rev. B* **2013**, *87*, 115106.

[12] S. Safaei, P. Kacman, R. Buczko, *Phys. Rev. B - Condens. Matter Mater. Phys.* **2013**, *88*, 045305.

[13] M. Z. Hasan, C. L. Kane, *Rev. Mod. Phys.* **2010**, *82*, 3045.

[14] X. L. Qi, S. C. Zhang, *Rev. Mod. Phys.* **2011**, *83*, 1057.

[15] T. H. Hsieh, H. Lin, J. Liu, W. Duan, A. Bansil, L. Fu, *Nat. Commun.* **2013**, *4*, 1901.

[16] E. Tang, L. Fu, *Nat Phys* **2014**, *10*, 964.

[17] M. Serbyn, L. Fu, *Phys. Rev. B - Condens. Matter Mater. Phys.* **2014**, *90*, 1.

[18] J. Liu, T. H. Hsieh, P. Wei, W. Duan, J. Moodera, L. Fu, *Nat. Mater.* **2013**, *13*, 178.

[19] S. Safaei, M. Galicka, P. Kacman, R. Buczko, *New J. Phys.* **2015**, *17*, 063041.

[20] B. A. Assaf, F. Katmis, P. Wei, C. Z. Chang, B. Satpati, J. S. Moodera, D. Heiman, *Phys. Rev. B - Condens. Matter Mater. Phys.* **2015**, *91*, 1.

[21] I. Zeljkovic, K. L. Scipioni, D. Walkup, Y. Okada, W. Zhou, R. Sankar, G. Chang, Y. J. Wang, H. Lin, A. Bansil, F. Chou, Z. Wang, V. Madhavan, *Nat. Commun.* **2015**, *6*, 6559.

[22] C. W. Niu, Y. Dai, Y. D. Ma, L. Yu, B. B. Huang, *Mater. Express* **2013**, *3*, 159.

[23] X. Qian, L. Fu, J. Li, *Nano Res.* **2015**, *8*, 967.

[24] I. Zeljkovic, Y. Okada, M. Serbyn, R. Sankar, D. Walkup, W. Zhou, J. Liu, G. Chang, Y. J. Wang, M. Z. Hasan, F. Chou, H. Lin, A. Bansil, L. Fu, V. Madhavan, *Nat. Mater.* **2015**, *14*, 318.

[25] E. Plekhanov, P. Barone, D. Di Sante, S. Picozzi, *Phys. Rev. B - Condens. Matter Mater. Phys.* **2014**, *90*, 161108(R).

[26] C. Fang, M. J. Gilbert, B. A. Bernevig, *Phys. Rev. Lett.* **2014**, *112*, 046801.

[27] A. R. Mellnik, J. S. Lee, A. Richardella, J. L. Grab, P. J. Mintun, M. H. Fischer, A. Vaezi, A. Manchon, E. A. Kim, N. Samarth, D. C. Ralph, *Nature* **2014**, *511*, 449.

[28] H. Guo, C. H. Yan, J. W. Liu, Z. Y. Wang, R. Wu, Z. D. Zhang, L. L. Wang, K. He, X. C. Ma, S. H. Ji, W. H. Duan, X. Chen, Q. K. Xue, *APL Mater.* **2014**, *2*, 0.

[29] C. Yan, J. Liu, Y. Zang, J. Wang, Z. Wang, P. Wang, Z.-D. Zhang, L. Wang, X. Ma, S. Ji, K. He, L. Fu, W. Duan, Q.-K. Xue, X. Chen, *Phys. Rev. Lett.* **2014**, *112*, 186801.

[30] C. M. Polley, P. Dziawa, A. Reszka, A. Szczerbakow, R. Minikayev, J. Z. Domagala, S. Safaei, P. Kacman, R. Buczko, J. Adell, M. H. Berntsen, B. M. Wojek, O. Tjernberg, B. J. Kowalski, T. Story, T. Balasubramanian, *Phys. Rev. B* **2014**, *89*, 075317.

[31] A. A. Taskin, F. Yang, S. Sasaki, K. Segawa, Y. Ando, *Phys. Rev. B - Condens. Matter Mater. Phys.* **2014**, *89*, 121302(R).

[32] B. A. Assaf, T. Phuphachong, V. V. Volobuev, A. Inhofer, G. Bauer, G. Springholz, L. A. de Vaulchier, Y. Guldner, *Sci. Rep.* **2016**, *6*, 20323.

[33] Y. Tanaka, T. Shoman, K. Nakayama, S. Souma, T. Sato, T. Takahashi, M. Novak, K. Segawa, Y. Ando, *Phys. Rev. B - Condens. Matter Mater. Phys.* **2013**, *88*, 235126.

[34] C.-H. Yan, H. Guo, J. Wen, Z.-D. Zhang, L.-L. Wang, K. He, X.-C. Ma, S.-H. Ji, X. Chen, Q.-K. Xue, *Surf. Sci.* **2014**, *621*, 104.

[35] T. Rauch, M. Flieger, J. Henk, I. Mertig, *Phys. Rev. B* **2013**, *88*, 245120.

[36] K. Ishizaka, M. S. Bahramy, H. Murakawa, M. Sakano, T. Shimojima, T. Sonobe, K. Koizumi, S. Shin, H. Miyahara, a Kimura, K. Miyamoto, T. Okuda, H. Namatame, M. Taniguchi, R. Arita, N. Nagaosa, K. Kobayashi, Y. Murakami, R. Kumai, Y. Kaneko, Y. Onose, Y. Tokura, *Nat. Mater.* **2011**, *10*, 521.

[37] A. Crepaldi, L. Moreschini, G. Autes, C. Tournier-Colletta, S. Moser, N. Virk, H. Berger, P. Bugnon, Y. J. Chang, K. Kern, A. Bostwick, E. Rotenberg, O. V. Yazyev, M. Grioni, *Phys. Rev. Lett.* **2012**, *109*, 096803.

[38] M. Sakano, M. S. Bahramy, A. Katayama, T. Shimojima, H. Murakawa, Y. Kaneko, W. Malaeb, S. Shin, K. Ono, H. Kumigashira, R. Arita, N. Nagaosa, H. Y. Hwang, Y. Tokura, K. Ishizaka, *Phys. Rev. Lett.* **2013**, *110*, 107204.

[39] A. Manchon, H. C. Koo, J. Nitta, S. M. Frolov, R. A. Duine, *Nat Mater* **2015**, *14*, 871.

[40] G. Springholz, in *Lead Chalcogenides Phys. Appl.* (Ed.: D. Khokhlov), Taylor & Francis, **2003**, pp. 123–207.

[41] P. H. O. Rappl, H. Closs, S. O. Ferreira, E. Abramof, C. Boschetti, P. Motisuke, A. Y. Ueta, I. N. Bandeira, *J. Cryst. Growth* **1998**, *191*, 466.

[42] A. Y. Ueta, G. Springholz, F. Schinagl, G. Marschner, G. Bauer, *Thin Solid Films* **1997**, *306*, 320.

[43] D. L. Partin, C. M. Thrush, S. J. Simko, S. W. Gaarenstroom, *J. Appl. Phys. J. Appl. Phys* **1989**, *66*, 6115.

[44] T. Ikeda, M. B. Toussaint, K. Bergum, S. Iwanaga, G. Jeffrey Snyder, *J. Mater. Sci.* **2011**, *46*, 3846.

[45] G. Springholz, A. Y. Ueta, N. Frank, G. Bauer, *Appl. Phys. Lett.* **1996**, *69*, 2822.

[46] G. Springholz, G. Bauer, *J. Appl. Phys.* **1995**, *77*, 540.

[47] P. J. McCann, J. Fuchs, Z. Feit, C. G. Fonstad, *J. Appl. Phys.* **1987**, *62*, 2994.

[48] V. L. Deringer, R. Dronskowski, *ChemPhysChem* **2013**, *14*, 3108.

[49] C. R. Hewes, M. S. Adler, S. D. Senturia, *J. Appl. Phys.* **1973**, *44*, 1327.

[50] Z.-H. Zhu, G. Levy, B. Ludbrook, C. N. Veenstra, J. A. Rosen, R. Comin, D. Wong, P. Dosanjh, A. Ubaldini, P. Syers, N. P. Butch, J. Paglione, I. S. Elfimov, A. Damascelli, *Phys. Rev. Lett.* **2011**, *107*, 186405.

[51] T. Valla, Z.-H. Pan, D. Gardner, Y. S. Lee, S. Chu, *Phys. Rev. Lett.* **2012**, *108*, 117601.

[52] L. A. Wray, S.-Y. Xu, Y. Xia, D. Hsieh, A. V Fedorov, Y. S. Hor, R. J. Cava, A. Bansil, H. Lin, M. Z. Hasan, *Nat. Phys.* **2011**, *7*, 32.

[53] P. D. C. King, R. C. Hatch, M. Bianchi, R. Ovsyannikov, C. Lupulescu, G. Landolt, B. Slomski, J. H. Dil, D. Guan, J. L. Mi, E. D. L. Rienks, J. Fink, A. Lindblad, S. Svensson, S. Bao, G. Balakrishnan, B. B. Iversen, J. Osterwalder, W. Eberhardt, F. Baumberger, P. Hofmann, *Phys. Rev. Lett.* **2011**, *107*, 096802.

[54] H. M. Benia, C. Lin, K. Kern, C. R. Ast, *Phys. Rev. Lett.* **2011**, *107*, 177602.

[55] S.-Y. Xu, Y. Xia, L. A. Wray, S. Jia, F. Meier, J. H. Dil, J. Osterwalder, B. Slomski, A. Bansil, H. Lin, R. J. Cava, M. Z. Hasan, *Science (80-.).* **2011**, *332*, 560.

[56] L. A. Wray, S.-Y. Xu, Y. Xia, D. Qian, A. V Fedorov, H. Lin, A. Bansil, Y. S. Hor, R. J. Cava, M. Z. Hasan, *Nat. Phys.* **2011**, *6*, 13.

[57] D. Hsieh, Y. Xia, D. Qian, L. Wray, J. H. Dil, F. Meier, J. Osterwalder, L. Patthey, J. G. Checkelsky, N. P. Ong, A. V Fedorov, H. Lin, A. Bansil, D. Grauer, Y. S. Hor, R. J. Cava, M. Z. Hasan, *Nature* **2009**, *460*, 1101.

[58] T. Arakane, T. Sato, S. Souma, K. Kosaka, K. Nakayama, M. Komatsu, T. Takahashi, Z. Ren, K. Segawa, Y. Ando, *Nat. Commun.* **2012**, *3*, 636.

[59] A. Varykhalov, G. Springholz, H. Steiner, R. Kirchschlager, G. Bauer, O. Caha, E. Schierle, E. Weschke, V. Holý, O. Rader, J. Sánchez-Barriga, A. Varykhalov, G. Springholz, H. Steiner, R. Kirchschlager, G. Bauer, O. Caha, E. Schierle, E. Weschke, A. A. Nal, S. Valencia, M. Dunst, J. Braun, H. Ebert, J. Minár, E. Golias, L. V Yashina, A. Ney, V. Hol, O. Rader, *Nat. Commun.* **2016**, *7*, 1.

[60] S. Picozzi, *Front. Phys.* **2014**, *2*, 1.

[61] D. Di Sante, P. Barone, R. Bertacco, S. Picozzi, *Adv. Mater.* **2013**, *25*, 509.

[62] M. Liebmann, C. Rinaldi, D. Di Sante, J. Kellner, C. Pauly, R. N. Wang, J. E. Boschker, A. Giussani, S. Bertoli, M. Cantoni, L. Baldrati, M. Asa, I. Vobornik, G. Panaccione, D. Marchenko, J. Sánchez-Barriga, O. Rader, R. Calarco, S. Picozzi, R. Bertacco, M. Morgenstern, *Adv. Mater.* **2016**, *28*, 560.

[63] J. Krempaský, H. Volfová, S. Muff, N. Pilet, G. Landolt, M. Radović, M. Shi, D. Kriegner, V. Holý, J. Braun, H. Ebert, F. Bisti, V. A. Rogalev, V. N. Strocov, G. Springholz, J. Minár, J. H. Dil, *http://arxiv.org/abs/1503.05004* **2015**.

[64] E. F. Schubert, *Doping in III–V Semiconductors*, Cambridge University Press, Cambridge, **1993**.

[65] C. Yan, J. Liu, Y. Zang, J. Wang, Z. Wang, P. Wang, Z.-D. Zhang, L. Wang, X. Ma, S. Ji, K. He, L. Fu, W. Duan, Q.-K. Xue, X. Chen, *Phys. Rev. Lett.* **2014**, *112*, 186801.

[66] C. R. Ast, J. Henk, A. Ernst, L. Moreschini, M. C. Falub, D. Pacile, P. Bruno, K. Kern, M. Grioni, *Phys. Rev. Lett.* **2007**, *98*, 186807.

[67] I. Gierz, F. Meier, J. H. Dil, K. Kern, C. R. Ast, *Phys. Rev. B* **1951**, *83*, 195122.

[68] *See Suppl. Mater. available online* **n.d.**

[69] S. D. Ganichev, E. L. Ivchenko, V. V. Bel'kov, S. A. Tarasenko, M. Sollinger, D. Weiss, W. Wegscheider, W. Prettl, *Nature* **2002**, *417*, 153.

[70] S. D. Ganichev, S. N. Danilov, P. Schneider, V. V. Bel'kov, L. E. Golub, W. Wegscheider, D. Weiss, W. Prettl, *J. Magn. Magn. Mater.* **2006**, *300*, 127.

[71] J. C. R. Sánchez, L. Vila, G. Desfonds, S. Gambarelli, J. P. Attané, J. M. De Teresa, C. Magén, A. Fert, *Nat. Commun.* **2013**, *4*, 2944.

[72] C. S. Lent, M. A. Bowen, J. D. Dow, R. S. Allgaier, O. F. Sankey, E. S. Ho, *Superlattices Microstruct.* **1986**, *2*, 491.

[73] M. P. Lopez Sancho, J. M. Lopez Sancho, J. Rubio, *J. Phys* **1985**, *15*, 851.

Tables:

Table 1. Rashba parameters of $Pb_{0.54}Sn_{0.46}Te$ (111) as a function of Bi-concentration n_{Bi} measured by ARPES at 110K (Figure 4), including Fermi energy E_F (relative to the top of the valence band), Rashba energy E_R, momentum splitting k_R, Rashba coupling constant $\alpha_R = 2E_R/k_R$ of the Rashba bands.

n_{Bi} [%]	E_F [*meV*]	E_R [*meV*]	k_R [$Å^{-1}$]	α_R [eVÅ]
0 %	–80	–	–	–
0.3 %	+140	13	0.011	2.4
0.7 %	+170	30	0.017	3.5
0.9 %	+190	38	0.022	3.8

Figures and figure captions:

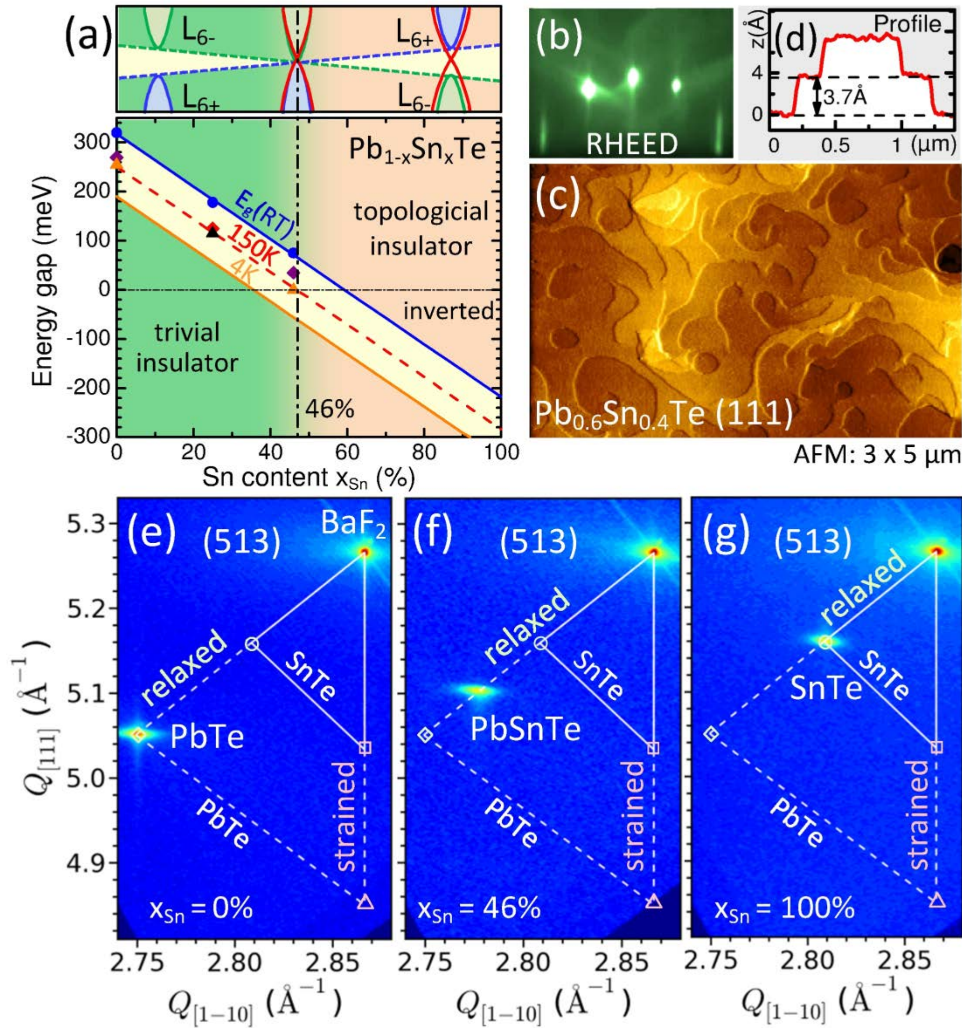

Figure 1: Basic properties of $Pb_{1-x}Sn_xTe$ (111) films. (a) Band gap in dependence of Sn content x_{Sn} at T = 300, 150 and 4K (solid/dashed lines) according to Refs. [[7],[8]]. Symbols: Our ARPES data for room temperature (●), 200K (◆), 150K (◆) and 100K (▲). The band inversion and trivial to non-trivial topological transition occurs at x_{Sn} = 0.36 and = 0.6 for 4K and 300K, respectively. (b,c) RHEED patterns and AFM image of a $Pb_{0.4x}Sn_{0.6}Te$ film grown by MBE on BaF_2 (111) substates. The extracted surface profile (d) shows only single monolayer steps with a height of 3.7 Å. (e-g) X-ray diffraction reciprocal space maps around the (513) Bragg reflection for three epilayers with x_{Sn}= 0, 0.46 and 1. As indicated, the layer peaks lie exactly on the line connecting the peak positions of bulk PbTe (◇) and SnTe (○), evidencing that all films are fully relaxed without residual lattice distortion. The expected peak positions of fully strained epilayers are indicated by (△,□).

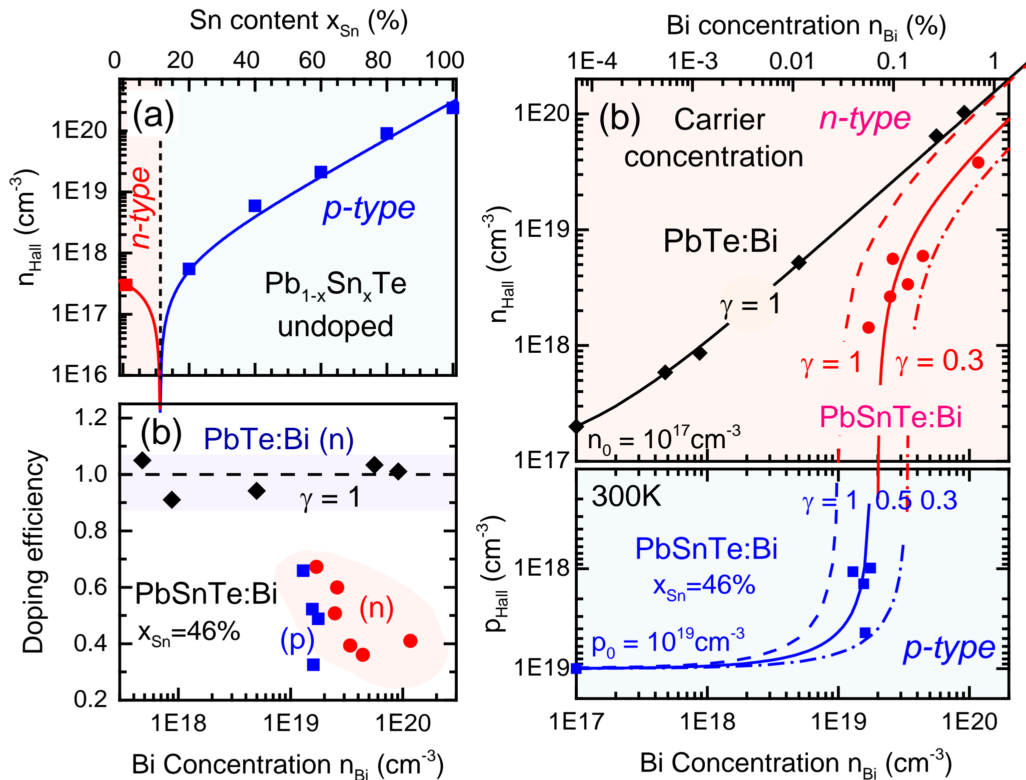

Figure 2: Effect of Bi-doping of TCI films. (a) Intrinsic carrier concentration of undoped $Pb_{1-x}Sn_xTe$ epilayers as a function of Sn content, revealing the high p-type character with increasing Sn content due to Sn vacancy formation. The solid line represents the fit of the experimental data assuming that the formation energy of vacancies decrease linearly with x_{Sn}. (b) Hall concentrations n_{Hall} obtained for PbTe:Bi (◆) and $Pb_{0.54}Sn_{46}Te$:Bi (■: p-type, ●n-type) as a function of Bi-dopand concentration. Solid lines: Expected n_{Hall} for different doping efficencies γ = 1 for PbTe (black line) and γ = 1, 0.5 and 0.3 for PbSnTe as indicated, based on the background carrier concentration measured for the undoped reference layers. (c) Bi-doping efficiency derived for PbTe (◆) and $Pb_{0.54}Sn_{46}Te$ (■: p-type, ● n-type) versus Bi concentration.

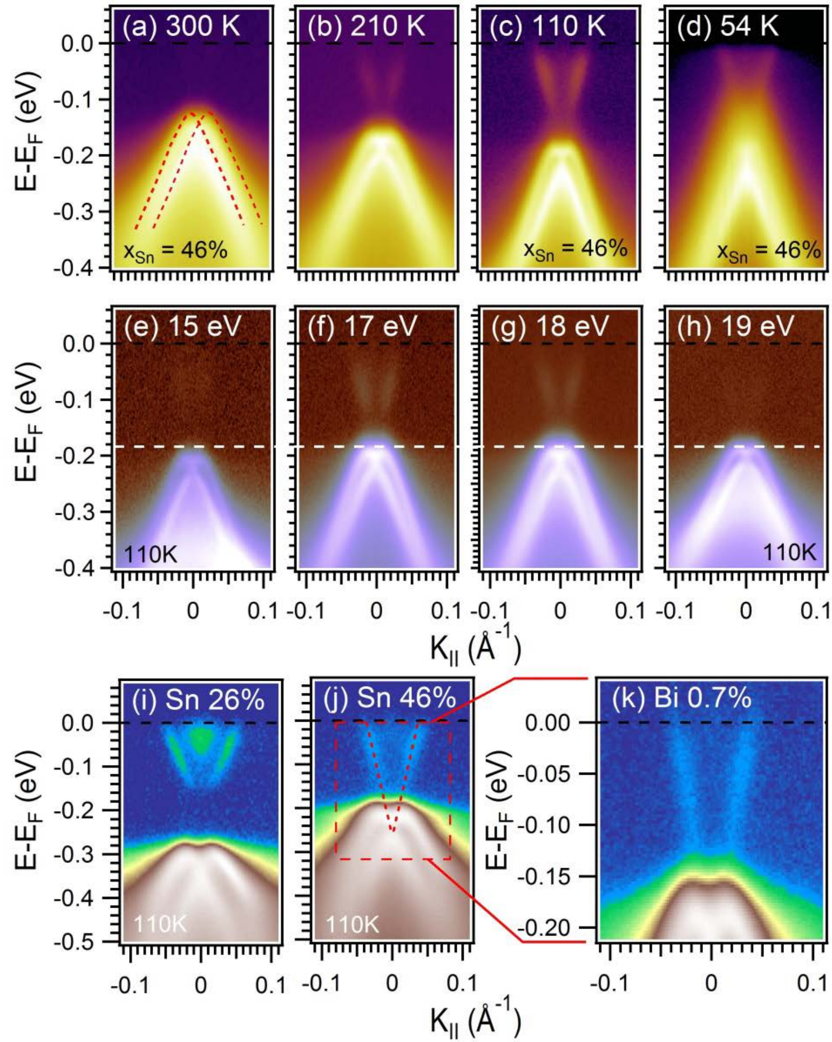

Figure 3: Topological phase transition characterized by ARPES. (a-d) Temperature dependent E(k) maps of a $Pb_{0.54}Sn_{0.46}Te$ (111) epilayer with 0.25% Bi measured around $\overline{\Gamma}$ of the surface BZ using a photon energy of 18 eV. The topological transition occurs at about 110 K. Below 80K photoemission becomes unstable due photon induced adsorption of residual gases and charging of the surface [[11]]. (e-g) Photon energy dependence measured at 110K. (i-k) ARPES spectra of $Pb_{1-x}Sn_xTe$ epilayers with low (x_{Sn} = 26%), respectively, high (46%) Sn content, demonstrating the trivial to non-trivial transition as a function of composition with an open gap for the former and closed gap for the latter at 110K. The intensity is shown on a logarithmic scale to reveal the TSS in the CB.

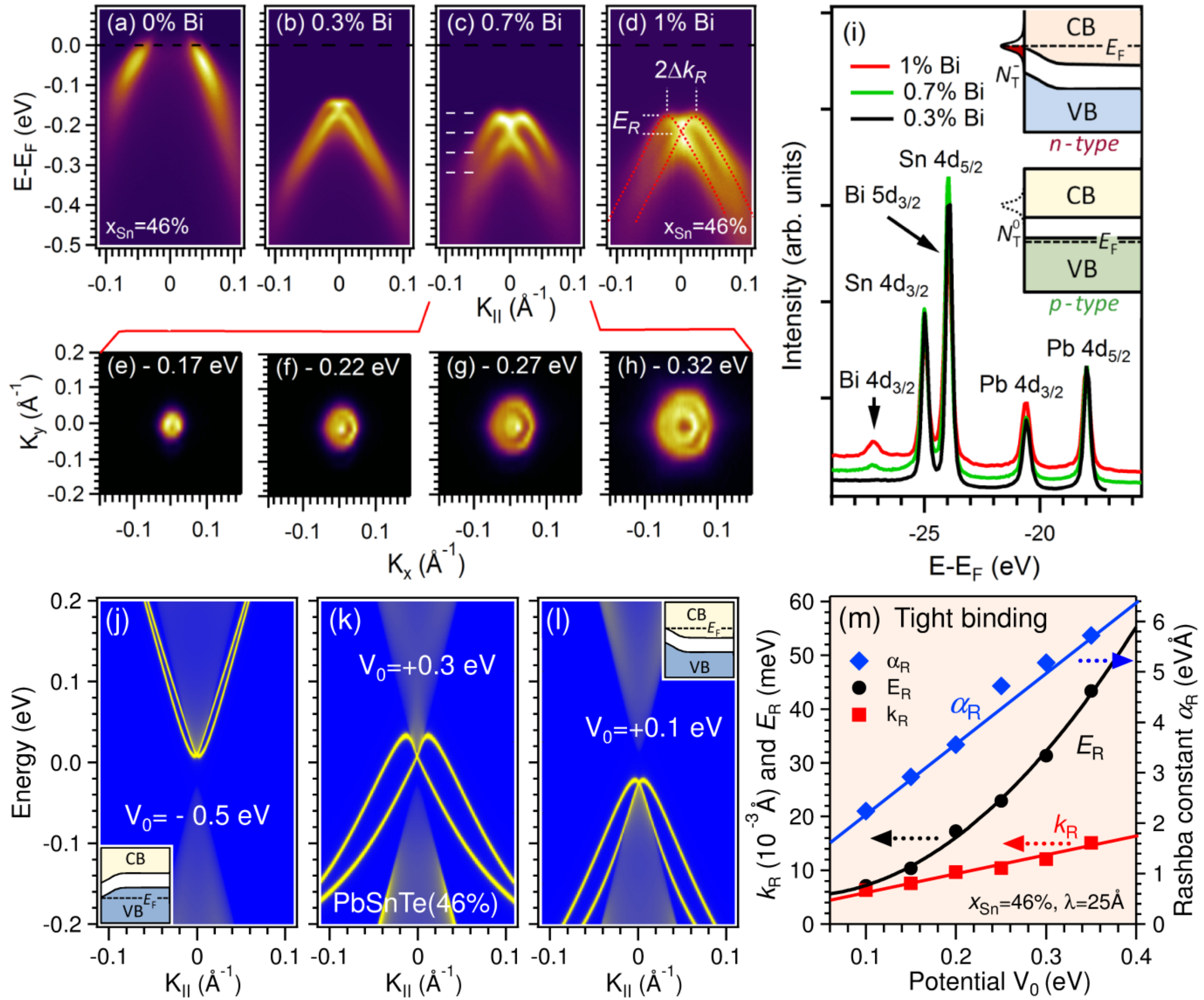

Figure 4: Effect of bulk Bi-doping on the Rashba effect. (a-d) ARPES spectra of $Pb_{0.54}Sn_{0.46}Te$ (111) with bulk Bi concentrations varying n_{Bi} = 0 to 1%, respectively, demonstrating effective tuning of the Fermi level and the strong increase of the Rashba splitting with Bi concentration. The ARPES maps were recorded around the $\bar{\Gamma}$-point at 100 K with a photon energy of 18 eV. The derivation of the Rashba constants α_R from the measured Δk_R and E_R is shown schematically in (d) and the results are listed in Table 1. (e-h) Constant energy contours at different binding energies for the sample with n_{Bi} = 0.7% showing the concentric rings of the Rashba bands and increasing hexagonal warping at lower energy. (i) Core level spectra excited with $h\nu$ = 90 eV showing the Bi $4d_{3/2}$ peak for increasing doping level. The upper insert illustrates the surface band bending induced by localized electron traps N_T^- at the surface that become populated with increasing bulk doping, whereas without Bi doping (lower insert) the traps are not occupied and no band bending occurs. (j-l) Tight binding supercell calculation of the Rasbha effect in $Pb_{0.54}Sn_{0.46}Te$ (111) induced by an upward (j) or downward (k,l) band bending towards the surface due to a negative, respectively, positive surface potential V_0. The screening length was set to λ = 25Å and T=200K. The Rashba constants derived from the calculations k_R (■), E_R (●) and $\alpha_R = 2E_R/k_R$ (◆) are plotted in (m) as a function of surface potential.